

Journal of Biomedical Optics

BiomedicalOptics.SPIEDigitalLibrary.org

Deciphering the internal complexity of living cells with quantitative phase microscopy: a multiscale approach

Cristina Martinez-Torres
Bastien Laperrousaz
Lotfi Berguiga
Elise Boyer-Provera
Juan Elezgaray
Franck E. Nicolini
Veronique Maguer-Satta
Alain Arneodo
Françoise Argoul

Deciphering the internal complexity of living cells with quantitative phase microscopy: a multiscale approach

Cristina Martinez-Torres,^{a,b} Bastien Laperrousaz,^{a,b,c} Lotfi Berguiga,^{b,d} Elise Boyer-Provera,^{a,b} Juan Elezgaray,^e Franck E. Nicolini,^{b,c,f} Veronique Maguer-Satta,^{b,c} Alain Arneodo,^{a,b} and Françoise Argoul^{a,b,*}

^aCNRS UMR5672, Laboratoire de Physique, Ecole Normale Supérieure de Lyon, 46 Allée d'Italie, 69007 Lyon, France

^bUniversité de Lyon 1, 43 Boulevard du 11 Novembre 1918, 69100 Villeurbanne, France

^cCNRS UMR5286, INSERM U1052, Centre de Recherche en Cancérologie de Lyon, 28 rue Laennec, 69008 Lyon, France

^dCNRS USR3010, Laboratoire Joliot-Curie, Ecole Normale Supérieure de Lyon, 46 Allée d'Italie, 69007 Lyon, France

^eCNRS UMR5248, Institut de Chimie et Biologie des Membranes et des Nano-objets, Allée de Geoffroy St Hilaire, 33600 Pessac, France

^fHospices Civils de Lyon, Hematology Department, Centre Hospitalier Lyon Sud, 165 Chemin du Grand Revoyet, 69495 Pierre Bénite, France

Abstract. The distribution of refractive indices (RIs) of a living cell contributes in a nonintuitive manner to its optical phase image and quite rarely can be inverted to recover its internal structure. The interpretation of the quantitative phase images of living cells remains a difficult task because (1) we still have very little knowledge on the impact of its internal macromolecular complexes on the local RI and (2) phase changes produced by light propagation through the sample are mixed with diffraction effects by the internal cell bodies. We propose to implement a two-dimensional wavelet-based contour chain detection method to distinguish internal boundaries based on their greatest optical path difference gradients. These contour chains correspond to the highest image phase contrast and follow the local RI inhomogeneities linked to the intracellular structural intricacy. Their statistics and spatial distribution are the morphological indicators suited for comparing cells of different origins and/or to follow their transformation in pathologic situations. We use this method to compare nonadherent blood cells from primary and laboratory culture origins and to assess the internal transformation of hematopoietic stem cells by the transduction of the BCR-ABL oncogene responsible for the chronic myelogenous leukemia. © 2015 Society of Photo-Optical Instrumentation Engineers (SPIE) [DOI: 10.1117/1.JBO.20.9.096005]

Keywords: quantitative phase microscopy; cellular complexity; wavelet transform; contour detection; refractive index.

Paper 150441R received Jun. 30, 2015; accepted for publication Jul. 31, 2015; published online Sep. 3, 2015.

1 Introduction

During the last several decades, identification of the physical properties of single living cells has been a subject of considerable interest for cytopathology diagnoses.^{1–5} In particular, quantitative optical microscopic methods^{3,6,7} have shown that the refractive index (RI) of a cell can be used as an indicator for cell transformation in cancer processes. By offering the possibility of recovering the global and local RIs of a living cell without any *a priori* treatment by staining agents,^{8–12} the development of quantitative phase microscopy (QPM) techniques is likely to shed a new light on the internal organization of different cell types.^{1,3,7,8,13–20} In addition to the measurements of the averaged RIs over the whole cells, the intracellular distribution of RIs revealed by QPM provides quantitative information concerning the internal heterogeneous complexity of living cells.^{8–12,21}

In recent years, cell imaging has seen the emergence of diverse microscopic setups suitable for living cell morphology capture.^{1,9,17,20,22,23} Among them, diffraction phase microscopy (DPM)^{23–25} has become a powerful tool for real-time analysis of single cell morphology and the alteration of cells in diverse pathologies.^{20,23,26} However, with the exception of enucleated mature red blood cells (RBCs), whose RI can be presupposed as homogeneous (at the resolution of optical microscopy), the extraction of RIs from phase images often requires the use of rather complex algorithms. Converting the optical phase computed from the

images of a QPM to an RI distribution in three dimensions (3-D) is quite impossible with a single wavelength measurement. Two-wavelength microscopes have been proposed to circumvent this limitation.²⁷ In some conditions, it is possible to include the effect of diffraction in the reconstruction process of high-resolution 3-D images throughout the entire sample volume.^{7,28,29} More recently, elegant and relatively simple and low-cost methods have been proposed^{30–32} for tomographic reconstruction of living cells. When the 3-D shape of the cell can be established *a priori*, the computation of RIs from phase images is then possible. Nonadherent cells in liquid generally adopt a spherical shape, which facilitates the inversion problem. We will use this assumption in this study for the characterization of blood cells.

Here, we aim at developing an original method for the detection of optical path difference (OPD) contours from living cells. The underlying idea is to look for local maxima of the OPD derivative in the two-dimensional (2-D) optical phase image. These maxima define interface chains where the RI and/or the cell shape vary abruptly and can be considered as domain boundaries. Even if we do not know *a priori* which is the prominent variation (RI or thickness) at each maximum, the connectivity of these maxima provides a direct access to the complexity of the cell interior. Because living cells are made of crowded macromolecules which may condensate or dilute at some stages

*Address all correspondence to: Françoise Argoul, E-mail: fargoul@ens-lyon.fr

of their lifespan, to assist global processes, such as growth, chromatin condensation, cell division, invasion, apoptosis, and migration, their internal structure bears a rather high level of complexity. Our study shows that except in some rare cases (RBCs), living blood cells are not partitioned into subdomains by isotropic and smooth contours, but rather look like randomly distributed contours with a broad distribution of lengths.

2 Materials and Methods

2.1 Diffraction Phase Microscope

Our DPM (Fig. 1) is directly inspired from the system published in Ref. 24. This interference microscope combines both off-axis and common-path interferometry techniques to produce fringe patterns [Fig. 1(a)] from which the phase images [Fig. 1(d)] can be reconstructed. The optical system is very compact and stable and does not require an expensive laser source [for instance, a laser-diode (Thorlabs, GmbH, Germany) with a wavelength $\lambda = 532$ nm]. It can be coupled to a fast image recording system (e.g., a CMOS camera, Hamamatsu, Japan, ORCA-Flash 4.0) with a 2048×2048 pixel grid. A Köhler illumination³³ is required to obtain an extremely even illumination and to avoid any perturbation of the sample image by the image of the light source at the image plane (IP) [Fig. 1(f)]. The interferences are obtained by combining a transmission grating (G) (110 grooves/mm), localized at the IP of the microscope, with a spatial filter (Thorlabs, custom-made) placed at the Fourier plane of lens L_1 that selects the first-order beam (imaging field) created by the grating and low-pass filters the zeroth-order

beam (reference). The two beams are recombined through a second Fourier lens L_2 . This $4f$ lens system adds a $5.9\times$ magnification ($f_1 = 25.4$ mm, $f_2 = 150$ mm). The spatial filter consists of two circular apertures with diameters of 1 and 15 μm [Fig. 1(f)]. The objective lens (O) $40\times$ (Olympus, SPlan40, NA = 0.7) allows a field of view of 75 μm . Prior to image capture, 65 μL of the solution containing the cells are poured between two glass coverslips glued by a Gene Frame Seal (Thermo Scientific AB-0577). Images are captured on the CMOS camera within the next 15 min of preparation at room temperature $T \sim 22^\circ\text{C}$. A reference image of the background next to the area containing the cell is also recorded for each image.

2.2 Cell Culture

2.2.1 Hematopoietic cell line model

The immature CD34+ TF1 cell line (ATCC CRL-2003) was maintained at 1×10^5 cells/mL in RPMI-1640 medium, 10% fetal calf serum, and granulocyte macrophage colony-stimulating factor (10 ng/mL) (Sandoz Pharmaceuticals). Engineered TF1-GFP and TF1-BCR-ABL-GFP cell lines were obtained by transduction with a murine stem cell virus-based retroviral vector, encoding either the enhanced green fluorescent protein (EGFP) cDNA alone as a control or the BCR/ABL-cDNA upstream from an IRES-eGFP sequence, as described in Ref. 34. EGFP+ TF1 cells were sorted using a Becton Dickinson FACSAria. For imaging, 65 μL of the solution were poured between two glass coverslips glued by a Gene Frame (ThermoScientific). The images were taken from two different

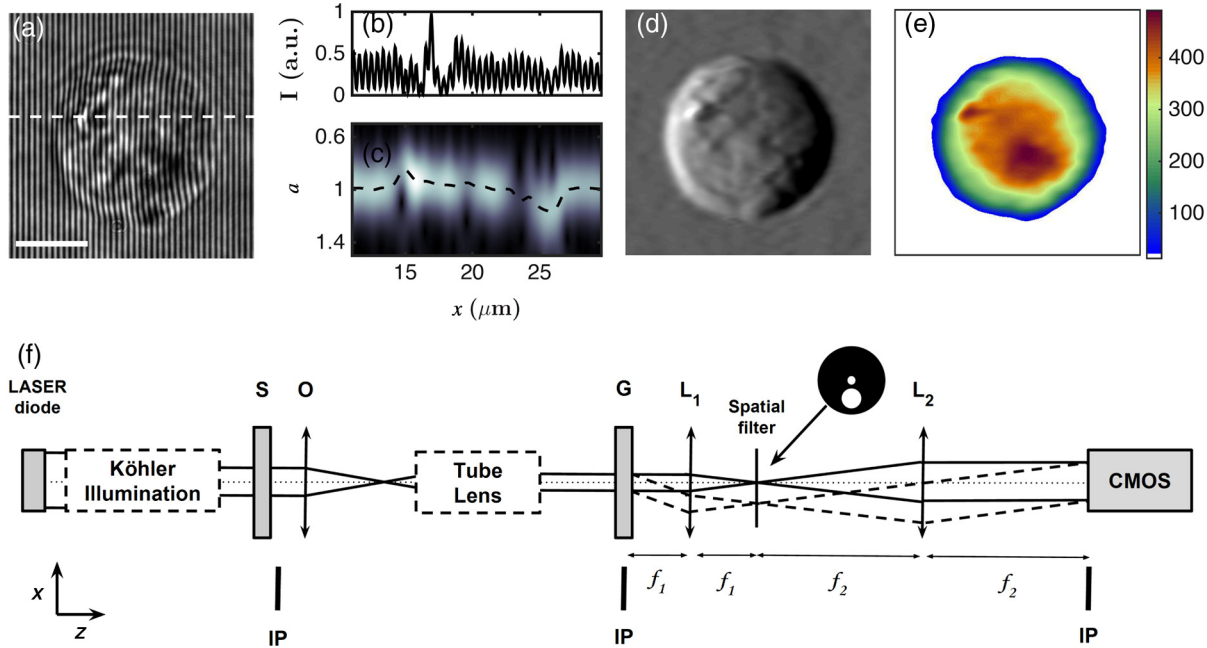


Fig. 1 Diffraction phase microscopy (DPM) principle: (a) untreated DPM image of a nonadherent immature myeloid cell (TF1-GFP). Scale bar: 5 μm ; (b) intensity profile of the section marked with a white dashed line in (a); (c) space-scale representation of the modulus of the wavelet transform (WT) $|\mathbf{T}_\Psi[f]|(b, a)$ of the section shown in (b); with a black dashed line we distinguish the wavelet transform modulus maxima (WTMM) profile. Note that we label the horizontal axis with the same variable x to align the two signals (image section and WT), in that representation $b = x$; (d) $\partial\phi(\mathbf{b})/\partial x$ computed for each line of the original phase image with the method illustrated in (c), the gray coding spans the interval $[-2.7$ to $5.4]$ rad/ μm ; (e) color-coded optical path difference (OPD) $\Phi = \phi\lambda/2\pi$ (in nm) computed from the arguments $A_\Psi[f](\mathbf{b}, a^*)$ of the WT at the scale a^* corresponding to a maximum of its modulus; and (f) DPM optical setup (see text).

cell batches per cell line type (TF1-GFP or TF1-BCR-ABL-GFP), and the total numbers of cells analyzed were 298 TF1-BCR-ABL-GFP (short name: TF1-BA) cells and 263 TF1-GFP cells.

2.2.2 Human primary cells (nucleated immature cells and red blood cells)

After informed consent in accordance with the Declaration of Helsinki and local ethics committee bylaws (from the Délégation à la recherche clinique des Hospices Civils de Lyon, Lyon, France), peripheral blood and bone marrow samples were obtained from chronic myelogenous leukemia patients. Mononuclear cells were separated using a Ficoll gradient (Bio-Whittaker) and were then subjected to CD34 immunomagnetic separation (Stemcell Technologies). The purity of the CD34+-enriched fraction was checked by flow cytometry and was over 95% on average.

3 Diffraction Phase Microscopy Image Analysis with a Wavelet-Based Multiscale Analyzing Method

3.1 Diffraction Phase Microscopy Principle for Cell Imaging

DPM^{23–25} allows a fast, nonintrusive, and high-sensitive measurement of the OPD produced by a transparent object embedded inside a homogeneous medium. The DPM optical setup sketched in Fig. 1(f) produces 2-D images with parallel fringe patterns [Fig. 1(a)] corresponding to a periodic modulation of the intensity:

$$I(\mathbf{x}) = P(\mathbf{x}) + Q(\mathbf{x}) \cos[f_g x + \phi(\mathbf{x})], \quad (1)$$

where $\phi(\mathbf{x})$ is the optical phase due to light transmission through the object at point $\mathbf{x} = (x, y)$, $P(\mathbf{x})$ and $Q(\mathbf{x})$ are, respectively, the unmodulated and modulated intensities at the same point of the image, and f_g is the spatial frequency of the diffraction grating. One common assumption is that $P(\mathbf{x})$ and $Q(\mathbf{x})$ vary much more slowly than $\phi(\mathbf{x})$.^{9,17,20,23,26} However, this is rarely the case with thick spherical cells, since they produce modulations of both the optical phase ϕ and the amplitude Q [Figs. 1(a) and 1(b)]. To circumvent this difficulty, we computed the ridges [wavelet transform modulus maxima (WTMM) lines] from the wavelet transform (WT) of the fringe image with a 2-D anisotropic Morlet analyzing wavelet.^{35–40} The implementation of this method on DPM has been recently published³⁶ and shown to surpass more traditional Hilbert methods⁴¹ when the amplitude modulation $Q(\mathbf{x})$ spans the frequencies that mix with the carrier frequency (f_g). In Fig. 1(c), we show the space-scale representation of the WT modulus computed from the horizontal section [Fig. 1(b)] of the fringe image in Fig. 1(a) ($a = 1$ corresponds to the fringe carrier frequency). The black dashed line outlines the position of the WTMM line. The scale a of the WTMM is proportional to the inverse of the derivative of the object phase $\{\partial[f_g x + \phi(\mathbf{x})]/\partial x\}$ and directly gives the image of the phase derivative shown in Fig. 1(d). The optical phase ϕ at position \mathbf{x} is given by the integral:

$$\phi(\mathbf{x}) = \frac{2\pi}{\lambda} \int_{z_m(\mathbf{x})}^{z_M(\mathbf{x})} \Delta n(\mathbf{x}, z) dz, \quad (2)$$

where λ is the illumination wavelength, $\Delta n = n - n_0$ is the difference between the RIs of the object (n) and the external medium (n_0), and z_M (respectively, z_m) is the upper (respectively, lower) bound of the object at position \mathbf{x} . The total thickness of the object at point \mathbf{x} is $h(\mathbf{x}) = z_M(\mathbf{x}) - z_m(\mathbf{x})$. The recovery of $\Delta n(\mathbf{x})$ from the phase map $\phi(\mathbf{x})$ amounts to solving an inverse problem.^{21,42} This is quite difficult without any assumption on the topography of the object, except in the case where the internal RI of the object is constant. This actually occurs for RBCs, for which we will be able to recover the shape of the cell from its fringe pattern²⁶ (see below). Nucleated cells involve a much more heterogeneous internal structure that requires a more complex reconstruction algorithm. Given that the optical phase ϕ depends on the illumination wavelength, in practice it is more convenient to work with the OPD: $\Phi = \phi\lambda/2\pi$. The OPD is equivalent to the retardation path length of the light after crossing the cell. According to Eq. (2), the OPD function is the integral on the RI drop through the cell whose limits of integration depend on the point \mathbf{x} :

$$\begin{aligned} \Phi(\mathbf{x}) &= \int_{z_m(\mathbf{x})}^{z_M(\mathbf{x})} \Delta n(\mathbf{x}, z) dz = [\Delta N(\mathbf{x}, z)]_{z_m(\mathbf{x})}^{z_M(\mathbf{x})} \\ &= \Delta N(\mathbf{x}, z_M) - \Delta N(\mathbf{x}, z_m), \end{aligned} \quad (3)$$

where $\Delta N(\mathbf{x}, z)$ is the integral function of $\Delta n(\mathbf{x}, z)$. For example, if $\Delta n(\mathbf{x}, z) = C^{st}$, $\Delta N(\mathbf{x}, z) = C^{st}z + B$ is a linear function of the variable z and $\Phi(\mathbf{x}) = C^{st}[z_M(\mathbf{x}) - z_m(\mathbf{x})] = C^{st}h(\mathbf{x})$. The OPD function precisely follows the shape of the object and its derivative is proportional to the derivative of its thickness h at each point \mathbf{x} . In general, the derivative of Φ along a radial coordinate of the (x, y) plane results from both RI and topography variations:

$$\frac{\partial \Phi(\mathbf{x})}{\partial r} = \frac{\partial \Delta N(\mathbf{x}, z_M)}{\partial r} - \frac{\partial \Delta N(\mathbf{x}, z_m)}{\partial r}. \quad (4)$$

If Δn is an integrable function, the two integral values $\Delta N(\mathbf{x}, z_M)$ and $\Delta N(\mathbf{x}, z_m)$ exist and their derivatives with respect to r can be computed. The boundary of the object is precisely defined by an abrupt change in the RI slope at the interface between the interior and the exterior media. Because domain boundaries in biological matter are not very sharp, we will rather consider them as transitory zones with a sharpness described by the gradient of the OPD. The local maxima of this OPD spatial gradient will follow the boundary zones wherever they can be detected (external and internal). If we consider that the object is made of the assembly of different internal structures with RI variations, we will apply the same assumption as above for the domain boundary detection. The main difficulty will, therefore, be to correctly compute these spatial gradients and extract local maxima lines. If the maxima lines are closed, we will infer the existence of well-defined internal structures with a quite homogeneous composition. On the contrary, if the maxima lines are unclosed and randomly distributed curves, we will rather infer a more complex organization of the internal structure of the considered object.

3.2 Diffraction Phase Microscopy Analysis of Model Spherical Cells

Let us first consider as a theoretical example, a spherical object of radius R with a radial RI function varying from n_0 (the outer medium) to n_c (at the center of the sphere):

$$\Delta n(\mathbf{x}, z) = \begin{cases} |(R-r)/R|^\alpha \Delta n_C & \text{for } r \leq R, \\ 0 & \text{for } r > R, \end{cases} \quad (5)$$

with $r = \sqrt{x^2 + y^2 + z^2}$ the radial distance, $\Delta n_C = n_C - n_0$, and α a real positive exponent. We consider only the positive values of z [the object is symmetric in respect to the equatorial plane (x, y)]. The boundaries of the sphere at position \mathbf{x} are such that $x^2 + y^2 \leq R^2$ are

$$\begin{aligned} z_m(\mathbf{x}) &= -\sqrt{R^2 - (x^2 + y^2)} \quad \text{and} \\ z_M(\mathbf{x}) &= \sqrt{R^2 - (x^2 + y^2)}. \end{aligned} \quad (6)$$

Centering the three vector bases (\vec{e}_x , \vec{e}_y , and \vec{e}_z) at the center of the sphere ($x_C = 0$, $y_C = 0$, and $z_C = 0$), we plot in Fig. 2(a) the RI profile along the x ($y = 0$) axis in green for different values of the exponent α in Eq. (5), namely $\alpha = 0$ (solid line), 0.25 (dashed-dotted line), 0.5 (dotted line), and superimposed to the sphere height profile (black dashed-dotted line).

The OPD of this spherical object at position \mathbf{x} with $x^2 + y^2 \leq R^2$ is given by

$$\Phi(\mathbf{x}) = \Delta n_C \int_{-\sqrt{R^2 - (x^2 + y^2)}}^{\sqrt{R^2 - (x^2 + y^2)}} \left| \left(R - \sqrt{x^2 + y^2 + z^2} \right) / R \right|^\alpha dz. \quad (7)$$

The three OPD functions corresponding to $\alpha = 0, 0.25$, and 0.5 are plotted in green in Fig. 2(b) with the same line style as in Fig. 2(a). When the RI is increasing monotonously from the

border to the center of the sphere, the OPD $\Phi(x, y = y_C)$ retains a global single humped shape, with a nonlinearity that depends on the exponent α . The local maxima of the first derivative of the OPD functions with respect to x are close to the position of the sphere's border. Note also that the OPD functions are symmetrical with respect to the center of the sphere, retaining the centrosymmetry of the object. In that example, we have computed the first derivative of the OPD with a smoothing first derivative of a Gaussian function, as further used in the experimental situations reported hereafter. Thus, the slight shift of the maxima of the red curves $\partial\Phi/\partial x$ from the sphere borders (dashed blue line) is due to the smoothing scale of this Gaussian filtering.

To mimic an internal variation of the RI, we have constructed another structure with the same outer spherical shape, but containing an internal concentric spherical shell with a higher RI, the boundary of which also varies smoothly with the radius r :

$$\Delta n(\mathbf{x}, z) = \begin{cases} [|f(r)|^\alpha + \{\cos[2\pi f(r)] - 1\}^2/6] \Delta n_C & \text{for } r \leq R, \\ 0 & \text{for } r > R, \end{cases} \quad (8)$$

where $f(r) = [R - \sqrt{x^2 + y^2 + z^2}]/R$. As shown in Fig. 2(c), the corresponding RI profiles for $\alpha = 0, 0.25$ and 0.5 bear two supplementary local maxima at $x = -2 \mu\text{m}$ and $2 \mu\text{m}$, which are superimposed to the smoothly increasing profile [similar to those in Fig. 2(a)]. The corresponding Φ and $\partial\Phi/\partial x$ profiles plotted in Fig. 2(d) are very instructive, since they show that the combination of both the spherical shape and nonmonotonous RI profiles may lead to an unexpected behavior. In the situation

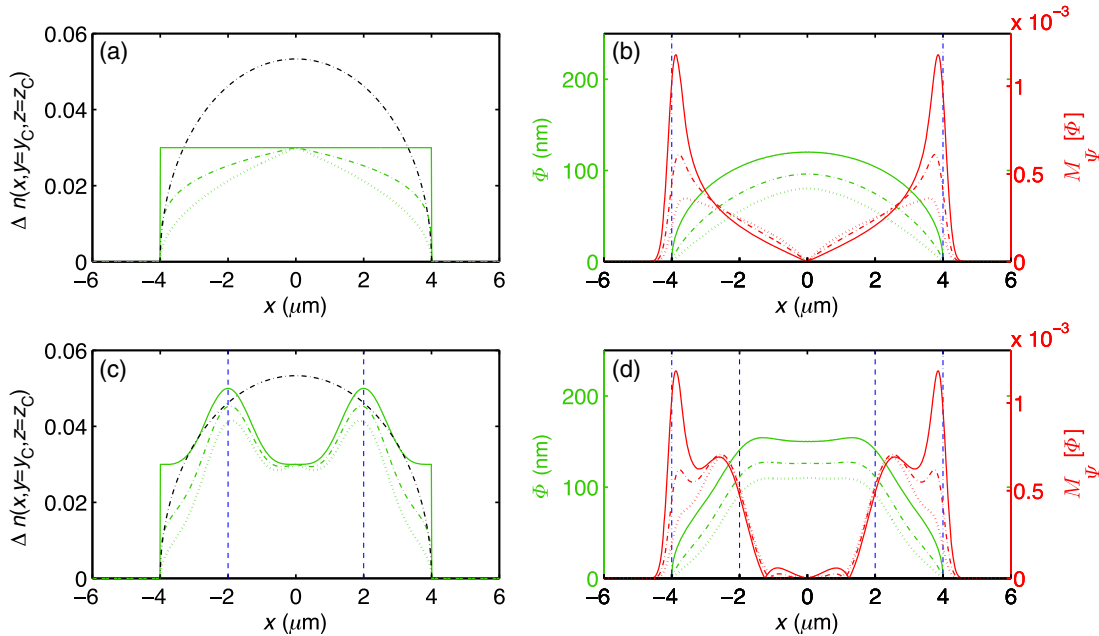


Fig. 2 OPD and OPD derivative functions for spherical shell models with radial RI profiles: (a) monotonously increasing (or constant) RI profiles $\Delta n(x, y = y_C, z = z_C)$ (from the border to the center) given by Eq. (5); (b) corresponding $\Phi(x)$ (green lines) and $\partial\Phi/\partial x$ (red lines) computed from the profiles in (a), using the first derivative of the Gaussian function as smoothing analysing wavelet (see text); (c) nonmonotonously increasing RI profiles $\Delta n(x, y = y_C, z = z_C)$ described by Eq. (8); and (d) $\Phi(x)$ (green lines) and $\partial\Phi/\partial x$ (red lines) computed as before from the profiles in (c). $\alpha = 0$ (respectively 0.25 and 0.5) is plotted with a green solid (respectively dashed-dotted and dotted) line. The underlying sphere shape is reported with a black dashed-dotted line. $x_C = 0$, $y_C = 0$, and $z_C = 0$ correspond to the center of the sphere.

shown here, not only the underlying object spherical shape is smeared out, but the local maxima of the index profile are also strongly damped, giving place to a quasi OPD plateau in the middle interval $[-2 \mu\text{m}, 2 \mu\text{m}]$; the higher α is, the flatter this plateau.

From this last model, we conclude that trusting the OPD isocountours to delineate regions of different RIs from a reconstructed phase image may be totally misleading even though we can still recover some information on the boundary (internal and external) properties with the computation of the local derivative of the OPD function.

3.3 Multiscale Method Based on the Continuous Two-Dimensional Wavelet Transform

Given that the OPD images are 2-D, computation of the derivatives must be performed along both directions \mathbf{x} and \mathbf{y} and ideally we must also include in the computation the possibility to smooth out the enhanced noise that could come from the derivative procedure. As originally noticed by Mallat and coworkers,^{43,44} the 2-D WT⁴⁵⁻⁴⁷ can be used to revisit Canny's multiscale edge detector.⁴⁸ The principle of this analysis is to smooth the image by convolving it with a filter and then to compute the gradient of the smoothed image. Let us consider the two wavelets defined respectively as the partial derivatives with respect to x and y of a 2-D smoothing function $\psi(\mathbf{x})$:

$$\Psi_1 = \frac{\partial\psi(\mathbf{x})}{\partial x} \quad \text{and} \quad \Psi_2 = \frac{\partial\psi(\mathbf{x})}{\partial y}. \quad (9)$$

The smoothing function ψ must be well localized (around $x = y = 0$), isotropic, and dependent on the modulus of \mathbf{x} only. The Gaussian function is the mostly used function that fulfills these conditions:

$$\psi(\mathbf{x}) = e^{-(x^2+y^2)/2}. \quad (10)$$

The WT of any 2-D function $\Phi(\mathbf{x})$ [which is embedded in $L^2(\mathcal{R}^2)$] with respect to the analyzing wavelets $\Psi = (\Psi_1, \Psi_2)$ has two components and can be expressed in a vectorial form:

$$\mathbf{T}_\Psi[\Phi](\mathbf{b}, a) = \begin{cases} T_{\Psi_1}[\Phi] = a^{-2} \int d^2x \Psi_1[a^{-1}(x - \mathbf{b})]\Phi(x) \\ T_{\Psi_2}[\Phi] = a^{-2} \int d^2x \Psi_2[a^{-1}(x - \mathbf{b})]\Phi(x) \end{cases}. \quad (11)$$

By a straightforward integration by parts,⁴⁵ this 2-D WT can be rewritten as

$$\begin{aligned} \mathbf{T}_\Psi[\Phi](\mathbf{b}, a) &= a^{-2} \nabla \left\{ \int d^2x \psi[a^{-1}(x - \mathbf{b})]\Phi(x) \right\} \\ &= \nabla \{ T_\psi[\Phi](\mathbf{b}, a) \} = \nabla \{ \psi_{b,a} * \Phi \}. \end{aligned} \quad (12)$$

If $\psi(\mathbf{x})$ is a smoothing filter like the Gaussian function [Eq. (10)], then Eq. (12) amounts to the computation of the gradient vector of $\Phi(\mathbf{x})$ smoothed by dilated versions $\psi(a^{-1}\mathbf{x})$ of this filter. If $\psi(\mathbf{x})$ has some vanishing moments, then $T_\psi[\Phi](\mathbf{b}, a)$ in Eq. (12) is the continuous 2-D wavelet (C2DWT) of $\Phi(\mathbf{x})$,³⁵ provided that $\psi(\mathbf{x})$ is an isotropic analyzing wavelet. Further on, we will compute the 2-D WT modulus $\mathcal{M}_\Psi[\Phi](\mathbf{b}, a)$ and its argument $\mathcal{A}_\Psi[\Phi](\mathbf{b}, a)$:

$$\begin{aligned} \mathcal{M}_\Psi[\Phi](\mathbf{b}, a) &= |\mathbf{T}_\Psi[\Phi](\mathbf{b}, a)|, \\ &= \{ [T_{\Psi_1}[\Phi](\mathbf{b}, a)]^2 + [T_{\Psi_2}[\Phi](\mathbf{b}, a)]^2 \}^{1/2}, \end{aligned} \quad (13)$$

and

$$\mathcal{A}_\Psi[\Phi](\mathbf{b}, a) = \text{Arg}[T_{\Psi_1}[\Phi](\mathbf{b}, a) + iT_{\Psi_2}[\Phi](\mathbf{b}, a)]. \quad (14)$$

In practice, at a given scale a , we first compute the 2-D fast Fourier transform (FFT) of Ψ_1 and Ψ_2 and we multiply these images by the FFT of Φ : $\tilde{\Psi}_1 \cdot \tilde{\Phi}$ and $\tilde{\Psi}_2 \cdot \tilde{\Phi}$ and from the inverse FFT of these products, we get the WTs $T_{\Psi_1}[\Phi]$ and $T_{\Psi_2}[\Phi]$. We then identify the so-called WTMM as the points \mathbf{b} , where the modulus $\mathcal{M}_\Psi[\Phi](\mathbf{b}, a)$ is locally maximum for a given scale a^* . To increase the resolution of this local maxima detection, we transform the pixelated images into radial representations. To switch from Cartesian to cylindrical geometry, we interpolate the WT argument and modulus on 1440 radial axes crossing the center of the cell with an angular shift of $\delta\theta = 4.410^{-3}$ rad. On each of these rotating axes with θ varying from 0 to 2π , we interpolate each pixelated image along the radial variable r with a spatial resolution $dr = 1.8$ nm. This allows a very acute determination of both the local angle θ and the argument \mathcal{A}_Ψ of the WT vector. From the radial coordinates of the WTMMs, we reconstruct maxima chains as 2-D curves made of a sequence of neighboring points (distant of less than $2r\delta\theta$).

When the maxima chain is circular [Fig. 3(a)] and the WT vector $\mathbf{T}_\Psi[\Phi](\mathbf{b}, a)$ is oriented outward [blue arrows in Fig. 3(a)], the argument of the WT is equal to the radial angle θ , $\Delta\theta = \mathcal{A}_\Psi[\Phi]_{\text{WTMM}} - \theta = 0$ [Fig. 3(b), blue circles]. If the WT vector is oriented inward [magenta arrows in [Fig. 3(a)], the argument is equal to π [Fig. 3(b), magenta circles].

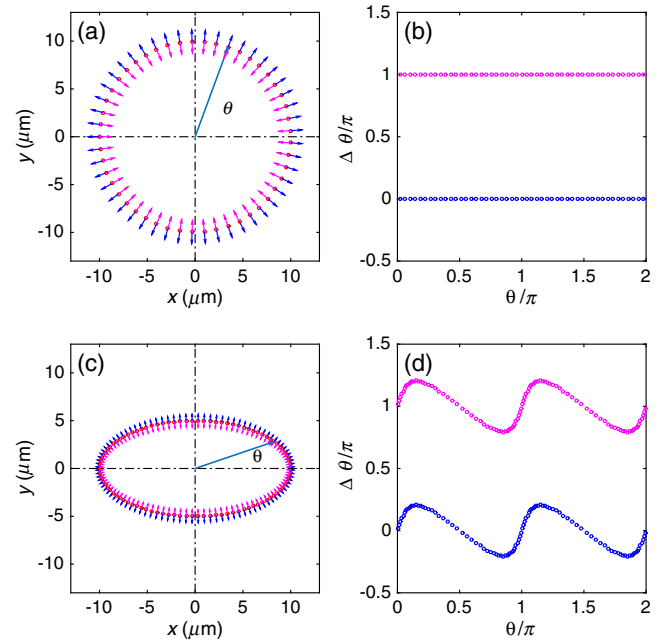


Fig. 3 WT argument for a spheroid and an ellipsoid cell model: (a) circular chain model with outward (respectively inward) WT vectors $[\mathbf{T}_\Psi[\Phi](\mathbf{r}, a)]$; (b) $\Delta\theta = \mathcal{A}_\Psi[\Phi]_{\text{WTMM}} - \theta$ on the WTMM chain line in (a); (c) ellipsoidal chain model with outward and inward wavelet vectors; and (d) $\Delta\theta = \mathcal{A}_\Psi[\Phi]_{\text{WTMM}} - \theta$ on the WTMM chain line in (c). The outward (respectively inward) vectors in (a) and (c) correspond to blue (respectively magenta) circles in (b) and (d).

we take an ellipsoidal-shaped maxima chain [Fig. 3(c)], the argument of the WT is no longer a constant function versus the angle θ . Again we consider the two cases of outward WT vector [blue arrows in Fig. 3(c) and blue circles in Fig. 3(d)] and inward WT vector [magenta arrows in Fig. 3(c) and magenta circles in Fig. 3(d)]. It is important to note that when the WTMM chain deviates from a circular contour, the angle difference $\Delta\theta$ may oscillate versus the radial angle θ , with alternating increasing ($\theta < 0.15\pi$) and decreasing ($0.15\pi < \theta < 0.85\pi$) intervals in Fig. 3(d). The flatter the shape of the chain, the larger the slope of these curves (in absolute values). The positive slopes of $\Delta\theta$ versus θ curves (which may reach vertical lines) correspond to highly curved chains (compared with a circle), whereas the negative slopes correspond to flatter chains (compared with a circle).

3.4 Wavelet-Based Analysis of Model Spherical Cells with Noise

We illustrate the WTMM method for detecting the local maxima chains from noisy data, taking again the previous model of a spherical object with an internal spherical shell of higher RI [Eq. (8)], adding a white noise term to the RI function before computing the OPD image:

$$\Delta n(\mathbf{x}, z) = \begin{cases} \{ |f(r)|^\alpha + \{ \cos[2\pi f(r)] - 1 \}^2 / 6 + \zeta \} \Delta n_C & \text{for } r \leq R, \\ \zeta & \text{for } r > R \end{cases} \quad (15)$$

ζ is a uniformly distributed random variable (MATLAB random generator rand) in the $[-1/10, 1/10]$ interval, giving a standard

deviation of ζ that we fix to 2.8%. We report in Fig. 4 the WT modulus and the local WTMM for two scales a of the analyzing wavelet computed from the noisy shell model [Eq. (15)]. From the OPD image [Fig. 4(d)] and its x -section through the central point ($x = x_C, y = y_C$) [Fig. 4(a), green line], we do not see much difference from the noise-free profile in Fig. 2(d). However, when computing the derivative with a small value of the scale parameter a [red curve in Fig. 4(a) and 2-D image of Fig. 4(b)], we notice that the background white noise that we have added to the RI introduces fluctuations that dramatically perturb the detection of the local maxima of the WT modulus [Fig. 4(c)]. To circumvent this problem, we follow a strategy recommended in Ref. 49 which amounts to increasing the scale parameter a until the number of local maxima chains no longer changes and their structure becomes more regular and robust. In that simple theoretical example, by simply increasing the scale a by a factor of 5 [Fig. 4(e)], we get the three expected maxima chain lines corresponding respectively to the outer boundary and the two (internal and external) boundaries on the internal concentric shell of a higher RI [Fig. 4(f)]. In this example, once the scale a is chosen correctly to smooth down the background noise, the maxima lines predicted by the model are recovered.

4 Application of the Wavelet Transform Modulus Maxima Method to Diffraction Phase Microscopy Images of Living Cells

To test the WTMM detection of phase boundary contours on DPM images of living cells, we first considered RBCs as an example of anucleated cells with an almost homogeneous cytoplasm (RI $\sim 1.401 \pm 0.006$)^{50–52} with a high concentration of hemoglobin. The shape of healthy, unstressed RBCs has been fully described in the literature^{26,52–55} with a biconcave equation

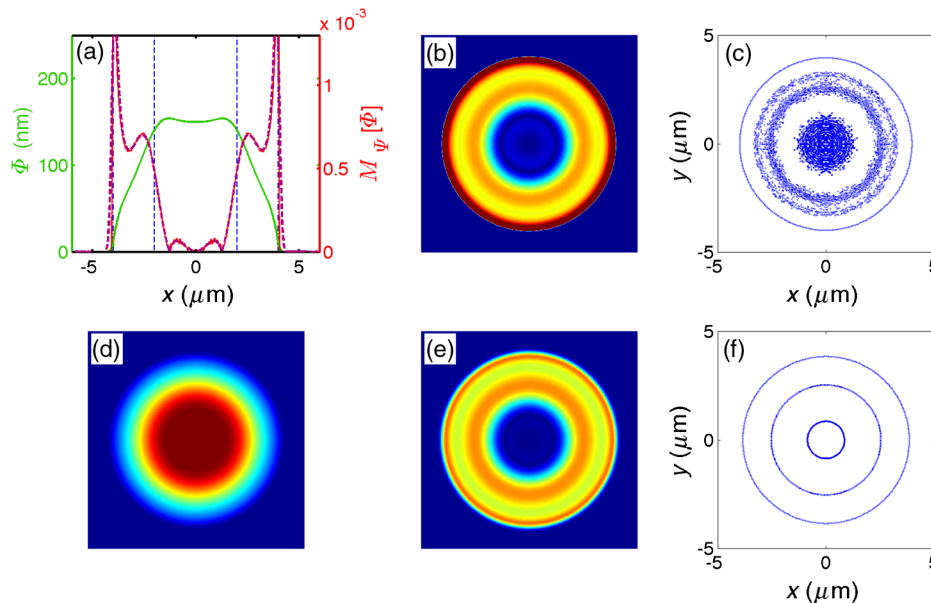


Fig. 4 WTMM chain line detection from the OPD of a spherical cell model with noise: (a) OPD $\Phi(x)$ (green line) computed from model [Eq. (15)] for $\alpha = 0.25$ and its WT modulus $\mathcal{M}_\psi[\Phi](b, a)$ estimated for two scales $a = 2$ (red) and 10 (magenta dashed line); (b) two-dimensional (2-D) color-coded image of $\mathcal{M}_\psi[\Phi]$ for $a = 2$, color coded from dark blue to red in the interval $[0, 0.001]$; (c) local maxima of $\mathcal{M}_\psi[\Phi]$ for $a = 2$; (d) 2-D color-coded representation of Φ (in the interval $[0, 133 \text{ nm}]$), computed from model [Eq. (15)]; (e) 2-D color-coded image of $\mathcal{M}_\psi[\Phi]$ for $a = 10$, color coded in the interval $[0, 0.001]$; and (f) local maxima of $\mathcal{M}_\psi[\Phi]$ for $a = 10$.

for their thickness h versus the radial coordinate r , as observed experimentally in isotonic buffers:

$$h(r) = z_M - z_m = \left[1 - \left(\frac{2r}{d} \right)^2 \right]^{1/2} \times \left[0.72 + 4.512 \left(\frac{2r}{d} \right)^2 - 3.426 \left(\frac{2r}{d} \right)^4 \right]. \quad (16)$$

4.1 Red Blood Cells

A typical healthy RBC has a maximum and minimum thicknesses of 2.84 and $1.44 \mu\text{m}$, respectively, and a diameter $d = 7.5 \pm 0.5 \mu\text{m}$. We recognize in Fig. 5(a) the characteristic OPD “donut” shape of a RBC,^{26,55} with a central hole and cylindrical symmetry. This example is particularly interesting to test the performance of WTMM detection method, as shown in Figs. 5(b)–5(d). Figure 5(c) shows the corresponding sections of Φ (green) and $\mathcal{M}_\psi[\Phi]$ (red) along the x direction, taken at the barycenter of the cell. The experimental green profile in Fig. 5(c) is in very good agreement with the biconcave shape (black line) predicted by Eq. (16). This method detects two WTMM chains, one exterior and one interior. Note that the exterior WTMM chain is color coded in hot (red to brown red) colors in Fig. 5(d) as an indicator of larger modulus values than the interior WTMM chain coded in cold (dark blue to blue) colors. The plot of the argument of the WT $\mathcal{A}_\psi[\Phi]$ versus θ along each of the two WTMM chains shows a clear separation of the two chains [Fig. 5(e)]. The exterior chain corresponds roughly to the diagonal (red to brown red color) and the interior chain is globally shifted from the diagonal by π . This shift corresponds simply to the inward direction of the wavelet vector (as already illustrated in Fig. 3). The two plots of the evolution of $\Delta\theta = \mathcal{A}_\psi[\Phi] - \theta$ in Fig. 5(f) for each WTMM chain confirm the reversal of the direction of the wavelet vector from the outer to

the inner WTMM chain. Indeed this vector gives the direction of the steepest descent of the WT modulus. More interestingly, we note that the fluctuations of $\Delta\theta$ on the inner chain are much larger than on the outer chain, meaning a more irregular shape (loss of circularity) distribution of the internal part of this cell. Given the predicted minimal thickness of a RBC,^{26,52–55} $h_{\min} \sim 1.44 \mu\text{m}$, we can use the averaged Φ values in the hole of this RBC $\Phi_{\min} = 90 \pm 5 \text{ nm} = h_{\min} \Delta n$ to estimate the RI drop: $\Delta n = 0.063 \pm 0.004$, leading to the following estimate of the RBC RI: $n = 1.333 + 0.063 = 1.396 \pm 0.004$.

4.2 Primary Immature Blood Cells

We consider now spherical mononucleated immature blood cells (nonadherent). These CD34+ cells are sorted from the bone marrow or peripheral blood by the CD34 antigen; they are a mixture of hematopoietic stem and progenitor cells with various degrees of maturity. In healthy conditions, these cells remain mostly in the bone marrow. In chronic myeloid leukemia (CML), these immature cells can also be found in the blood. These cells have a rather high nuclear:cytoplasmic ratio (N:C) in the interphase.^{56–58} This ratio indicates the maturity of the cell; for example for immature leukocytes, it may reach 4:1.⁵⁹ If we assume that the nucleus is a concentric sphere (which can be applied to CD34+ cells) of the cell of radius R_N , a 4:1 N:C would give $R_N = (4/5)^{1/3} \cdot R_C \sim 0.93 R_C$ (R_C is the cell radius). If $R_C = 4 \mu\text{m}$, this would give $R_N = 3.7 \mu\text{m}$, leaving only a 300-nm distance in between the outer cytoplasmic and the inner nuclear membranes. Such a large nucleus should not be distinguishable from the outer membrane shell in our microscope device, since one fringe produced by the grating is too thick $\sim 400 \text{ nm}$ (in the scale of the cell). If the N:C ratio drops to 3:1, the radius of the nucleus decreases only by 70 nm, which should also be undetectable with our optical setup. The impact of the nucleus should, therefore, only be visible on the amplitude of the OPD Φ and/or its derivative. However, we should be able to detect

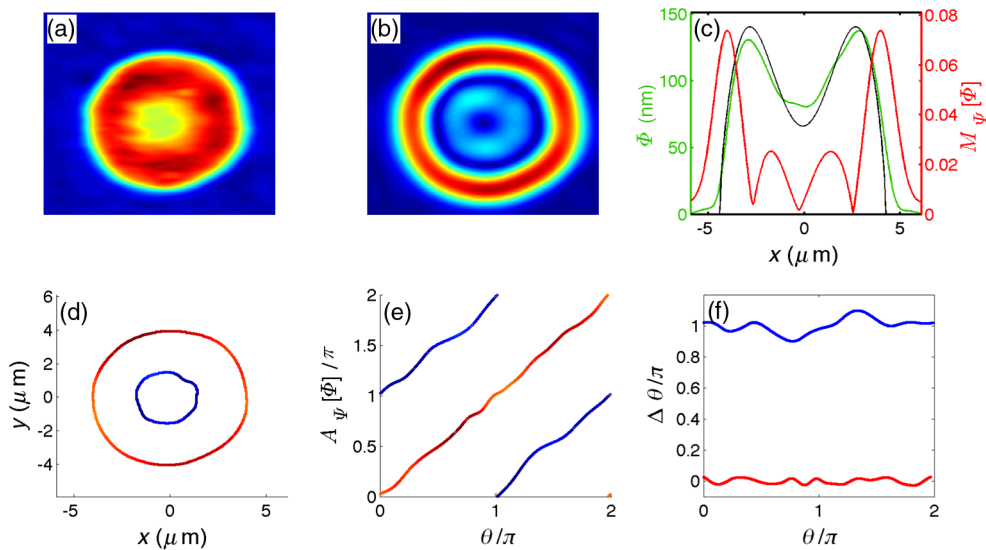


Fig. 5 WTMM chain detection from the OPD of a living red blood cell (RBC): (a) OPD phase image, color coded from dark blue ($\Phi = 0 \text{ nm}$) to brown red ($\Phi = 163 \text{ nm}$); (b) $\mathcal{M}_\psi[\Phi]$ (b, a) for $a = 15$, color coded in the interval $[0, 0.09]$; (c) horizontal sections through the barycenter of the cell of the OPD Φ (green line) and of $\mathcal{M}_\psi[\Phi]$ (red line). The black line corresponds to the biconcave shape predicted by Eq. (16); (d) WTMM chains of the RBC cell shown in (a), color coded according to the value of $\mathcal{M}_\psi[\Phi]$; (e) plot of the argument $\mathcal{A}_\psi[\Phi]_{\text{WTMM}}$ of the WTMM chains versus θ [same color coding as in (d)]; and (f) plot of $\Delta\theta = \mathcal{A}_\psi[\Phi]_{\text{WTMM}} - \theta$ versus θ .

internal structures of the nuclei on this type of cells. Figure 6 illustrates the WTMM boundary detection on a rounded nonadherent living CD34+ cell. The outer boundary of this spherical cell is detected straightforwardly by the maxima chain with maximum mean $\langle \mathcal{M}_\Psi[\Phi]_{\text{WTMM}} \rangle$. While the external contour of the cell is very circular [$\mathcal{A}_\Psi[\Phi]_{\text{WTMM}}$ versus θ is a straight line in Fig. 6(e)], with few fluctuations [Fig. 6(f)], the internal shape of Φ [Fig. 6(a)] presents a single slightly off-centered small bump, leading to the conical shape of the Φ profile in Fig. 6(c) (green line). If we fit the outer part of this Φ profile by the prediction for a homogeneous sphere with radius $R_C = 4.5 \pm 0.08 \mu\text{m}$ [$\alpha = 0$ in Eq. (7)]:

$$\Phi(x) = 2\Delta n_C \sqrt{R^2 - (x^2 + y^2)}, \quad (17)$$

we get the following estimate for its internal index: $n = 1.365 \pm 0.004$ [black line in Fig. 6(c)]. Another way to obtain an estimate of the internal cell index is to compute the optical path volume (OPV):

$$\text{OPV} = \int_{y_m}^{y_M} \int_{x_m}^{x_M} \int_{z_m(x)}^{z_M(x)} \Delta n(x, y, z) dz dx dy. \quad (18)$$

For the discretized Φ images, we simply compute

$$\text{OPV} = \mathcal{S}_{xy} \sum_{\text{intra}} \text{OPD}, \quad (19)$$

where \mathcal{S}_{xy} is the area of a pixel. For a homogeneous sphere with RI drop Δn , the OPV is that of an oblate ellipsoid with height $R\Delta n_C$ (z direction) and radius R in the (x, y) plane:

$$\text{OPV} = \frac{4}{3} \pi R_C^3 \Delta n_C = V_S \Delta n_C, \quad (20)$$

with V_S the formal volume of the perfect spherical cell of the same radius R_C . From the OPD image of Fig. 6(a), we obtain

$\text{OPV} = 13.84 \mu\text{m}^3$, which with $R_C = 4.5 \mu\text{m}$ leads to $\Delta n_C = 0.0365 \pm 0.005$ and thus to a cell averaged RI $n = 1.369 \pm 0.005$. This estimation is better when matching the averaged cell RI than the above estimation obtained from a single $\Phi(x)$ profile since it embraces the whole cell phase topography. Globally, we can conclude from this example that this primary blood cell has an average RI which is not much larger than what is known for eukaryotic cell cytoplasmic zones.⁶⁰ This OPV is an interesting quantity that will help us comparing different cells. In particular, by dividing this OPV [Eq. (20)] by the projected area of the cell to the power $3/2$: $S_C^{3/2} = (\sum_{\text{intra}} \mathcal{S}_{xy})^{3/2}$, we get a dimensionless quantity that can be computed to compare adherent and nonadherent cells:

$$\langle \Delta n_{\text{eff}} \rangle = \begin{cases} 3\sqrt{4\pi} & \text{OPV}/S_C^{3/2} \\ \Delta n_C, & \text{for spherical cells} \end{cases}. \quad (21)$$

This quantity gives the same prediction for the cell RI as previously estimated, if the cell is spherical. If the cell is not spherical, this quantity provides some estimate of the effective density of the cell and its flattening under adhesion; the flatter the cell the smaller $\langle \Delta n_{\text{eff}} \rangle$ gets.

The small off-centered dome of the CD34+ cell shown in Fig. 6 corresponds to a higher density zone of the nucleus which is mainly detectable by the WTMM method on its border oriented toward the center of the cell image (computed from the center of mass of the projected shadow of the cell image onto the \mathbf{x} plane, where its gradient is stronger). The outer contour of this small dome is shrouded in the nuclear-extracellular borders and is hardly detectable due to a limited number of fringes per micrometer.

It is interesting to compare this WTMM analysis of a domed CD34+ cell with a flatter CD34+ cell from the same bone marrow sample (Fig. 7). This new cell has an average radius of $5.53 \pm 0.18 \mu\text{m}$ and is only 23% larger than the previous CD34+ cell (Fig. 6). Its OPD topography is drastically different, since its internal nucleus is more inhomogeneous with a larger

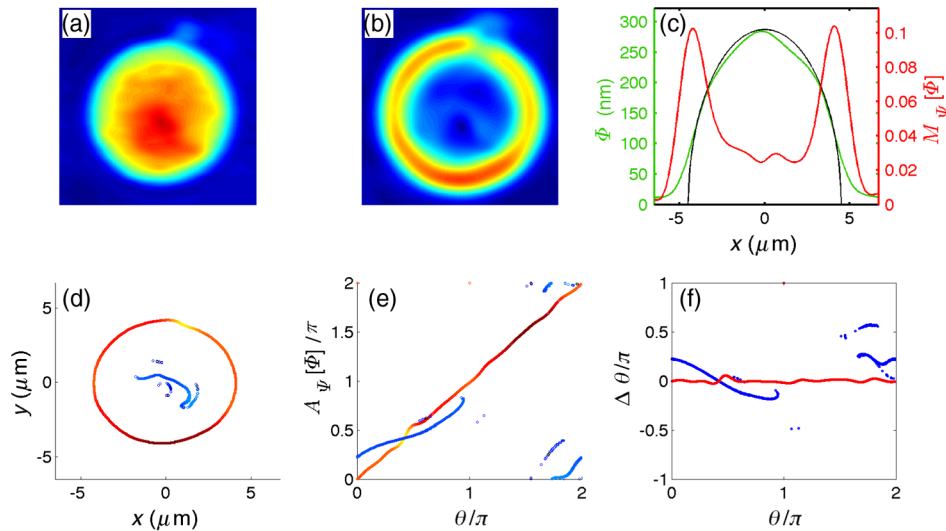


Fig. 6 WTMM method analysis of the OPD of a living domed CD34+ cell: (a) OPD phase image, color coded from dark blue ($\Phi = 0$ nm) to brown red ($\Phi = 320$ nm); (b) $\mathcal{A}_\Psi[\Phi]$ (b, a) for $a = 15$, color coded in the interval $[0, 0.16]$; (c) horizontal sections through the barycenter of the cell of the OPD Φ (green line) and of $\mathcal{A}_\Psi[\Phi]$ (red line). The black line corresponds to the OPD profile for a homogeneous sphere with radius $4.5 \mu\text{m}$ and index $n = 1.365$; (d) WTMM chains of the CD34+ cell shown in (a), color coded according to the value of $\mathcal{A}_\Psi[\Phi]$; (e) plot of the argument $\mathcal{A}_\Psi[\Phi]_{\text{WTMM}}$ of the WTMM chains versus θ [same color coding as in (d)]; and (f) plot of $\Delta\theta = \mathcal{A}_\Psi[\Phi]_{\text{WTMM}} - \theta$ versus θ .

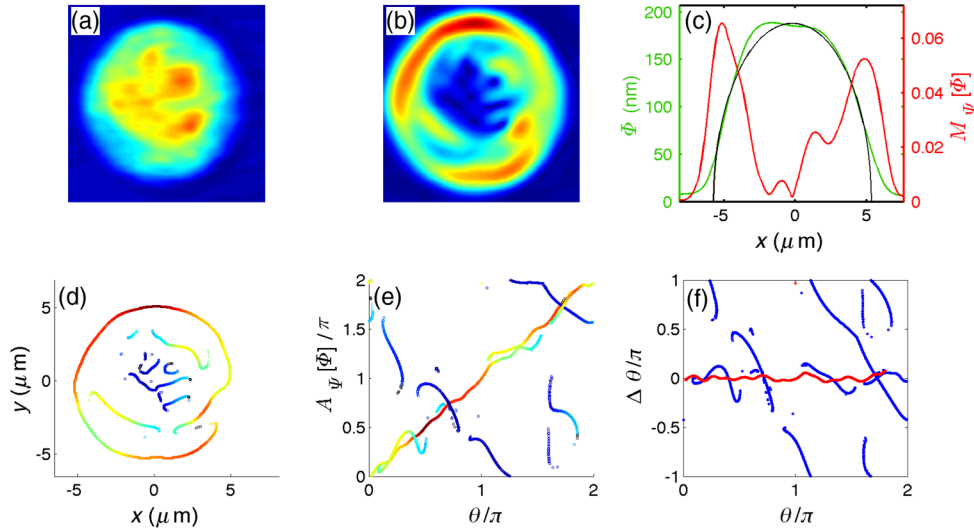


Fig. 7 WTMM method analysis of the OPD of a living flattened shape CD34+ cell: (a) OPD phase image, color coded from dark blue ($\Phi = 0$ nm) to brown red ($\Phi = 230$ nm); (b) $\mathcal{M}_\psi[\Phi](\mathbf{b}, a)$ for $a = 15$, color coded in the interval $[0, 0.092]$; (c) horizontal sections through the barycenter of the cell of the OPD Φ (green line) and of $\mathcal{M}_\psi[\Phi]$ (red line). The black line corresponds to the OPD profile for a homogeneous sphere with radius $5.53 \mu\text{m}$ and index $n = 1.35$; (d) WTMM chains of the CD34+ cell shown in (a), color coded according to the value of $\mathcal{M}_\psi[\Phi]$; (e) plot of the argument $\mathcal{A}_\psi[\Phi]_{\text{WTMM}}$ of the WTMM chains versus θ [same color coding as in (d)]; and (f) plot of $\Delta\theta = \mathcal{A}_\psi[\Phi]_{\text{WTMM}} - \theta$ versus θ .

set of WTMM chains. One may wonder if this roughening of the internal core of the cell could be accounted for by its larger size, which would facilitate the local maxima detection. Actually, the threshold for local maxima detection is chosen to be small enough (1×10^{-3}) to collect all the local events given the wavelet scale a . The occurrence of these WTMM chains is really reflecting a modification of the internal structure of the cell. Another way to confirm this transformation is to compare the OPVs: in that latter case, $\text{OPV} = 13.3 \mu\text{m}^3$, which, surprisingly, is very close to the OPV of the previous CD34+ cell. According to Eq. (20), if we divide the OPV by the volume of the ideal sphere with the same radius $R_C = 5.53 \mu\text{m}$ ($V_S = 708 \mu\text{m}^3$), we get an average RI drop: $\Delta n_C = 0.0188 \pm 0.005$, leading to a much smaller averaged RI of the cell: $n_C = 1.352 \pm 0.005$. Since the OPV remains invariant, we know that the total material of the cell is not changed. This means that its apparent surface and its internal structure have changed, possibly due to a local condensation of the intranuclear material. Since we did not stain the nucleus to avoid any alteration of the cell with an external agent that could also modify the interferometric measure, we cannot conclusively determine this possibility. Further experiments could be needed to confirm this hypothesis, in particular by following the transformation of a living cell during a whole division cycle.

4.3 Cell Models for Hematopoietic Stem Cells

Primary CD34+ cells are much more difficult to maintain alive than laboratory cell lines. We used the TF1 cell line as a model of immature CD34+ cells, because it displays clonogenic ability similar to human bone marrow CD34+ cells and is able to differentiate into myeloid lineages.⁶¹ As compared with a wild-type or GFP-transduced TF1 cells, BCR-ABL-transduced (CML oncogene) TF1 cells (TF1-BCR-ABL) increase their transcriptional levels of BCR-ABL and ABL.³⁴ These cells could bring information on the impact of BCR-ABL oncogene transduction on

immature cells. Figure 8 shows the results of the WTMM analysis of the OPD of a nontransformed (control) TF1-GFP cell. Immediately, we notice that the size of this cell ($R_C = 8.22 \pm 0.2 \mu\text{m}$) is definitely larger than that of the CD34+ primary cells. This cell looks rather homogeneous in its composition because we do not detect so many WTMM chains. The parametrization of the OPD section [Fig. 8(c)] and the computation of the OPV = $76 \mu\text{m}^3$ lead to a mean RI, $n_C = 1.363 \pm 0.004$, which is not very far from the one estimated for the first domed CD34+ cell (Fig. 6). It seems that even if this cell has significantly increased its size compared with primary cells, its optical properties are not very different. In the sampling of these control and transformed cells, we have observed very drastic changes, as illustrated in Fig. 9, for the TF1-GFP-BCR-ABL cell line whose morphology is dramatically different from the TF1-GFP cell shown in Fig. 8. This type of transformation occurs in less than 10% of the cells transduced by the BCR-ABL oncogene, but since it is accompanied by a drastic reorganization of the cytoskeleton, we think it is important to show how the QPM-WTMM method can interpret and quantify this transformation. BCR-ABL has previously been demonstrated to bind actin filaments (F-actin),⁶² one of the major force transducers in cellular adhesion and motility,⁶³ and to induce its redistribution into punctate, juxtanuclear aggregates,⁶⁴ implying a reorganization of the whole cytoskeleton. In Fig. 9, we immediately notice that the cell radius has increased by a factor $\sim 3/2$. The number of chains detected by the WTMM method has also increased by a factor ~ 5 (we count only the chains with a length larger than 100 nm, as smaller chain detection may be spoiled by background noise). The mean RI of this TF1-GFP-BCR-ABL cell, computed from the OPV/ V_S ratio [Eq. (20)], is not distinguishable from the mean RI of the previous TF1-GFP cell. When comparing Figs. 8(b) and 8(c) and 9(b) and 9(c), we realize that the difference between the 2-D OPD derivatives of control and cancer cells is higher in the inner cell structures ($\mathcal{M}_\psi[\Phi] = 0.011 \pm 0.009$ for TF1-GFP

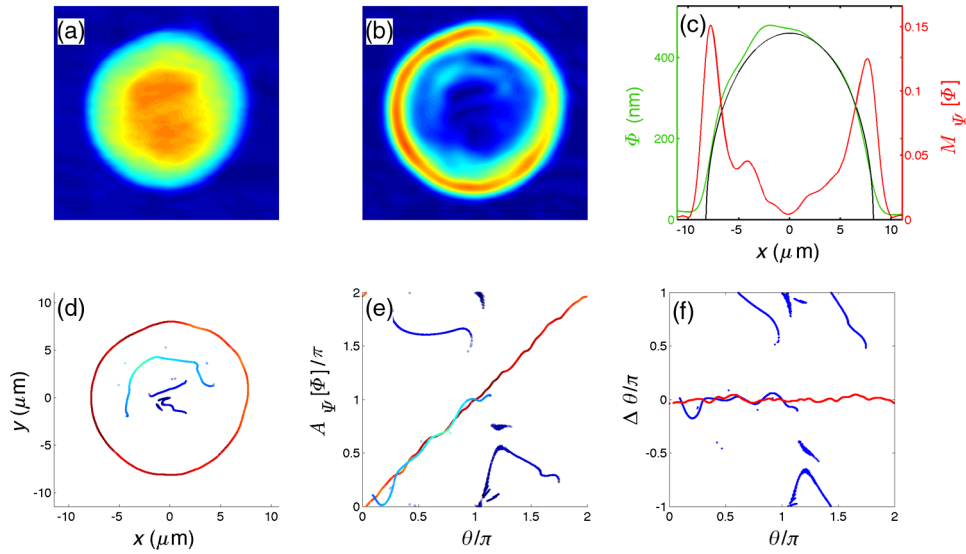


Fig. 8 WTMM method analysis of the OPD of a living hematopoietic model cell TF1-GFP: (a) OPD phase image, color coded from dark blue ($\Phi = 0$ nm) to brown red ($\Phi = 507$ nm); (b) $\mathcal{M}_\psi[\Phi](\mathbf{b}, \mathbf{a})$ for $a = 15$, color coded in the interval $[0, 0.2]$; (c) horizontal sections through the barycenter of the cell of the OPD Φ (green line) and of $\mathcal{M}_\psi[\Phi]$ (red line). The black line corresponds to the OPD profile for a homogeneous sphere with radius $8.22 \mu\text{m}$ and index $n = 1.363$; (d) WTMM chains of the TF1-GFP cell shown in (a), color coded according to the value of $\mathcal{M}_\psi[\Phi]$; (e) plot of the argument $\mathcal{A}_\psi[\Phi]_{\text{WTMM}}$ of the WTMM chains versus θ [same color coding as in (d)]; and (f) plot of $\Delta\theta = \mathcal{A}_\psi[\Phi]_{\text{WTMM}} - \theta$ versus θ .

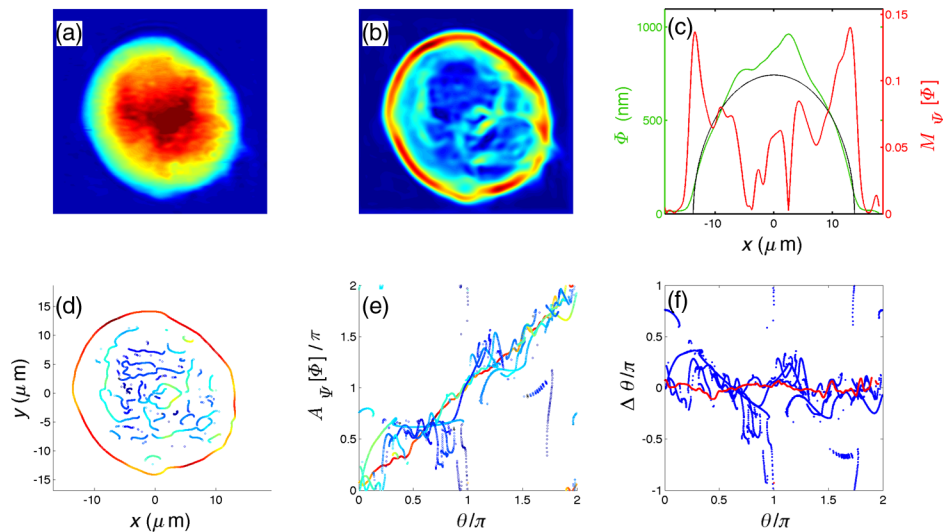


Fig. 9 WTMM method analysis of the OPD of a living TF1-BCR-ABL cell: (a) OPD phase image, color coded from dark blue ($\Phi = 0$ nm) to brown red ($\Phi = 1050$ nm); (b) $\mathcal{M}_\psi[\Phi](\mathbf{b}, \mathbf{a})$ for $a = 15$, color coded in the interval $[0, 0.2]$; (c) horizontal sections through the barycenter of the cell of the OPD Φ (green line) and of $\mathcal{M}_\psi[\Phi]$ (red line). The black line corresponds to the OPD profile for a homogeneous sphere with radius $13.77 \mu\text{m}$ and index $n = 1.36$; (d) WTMM chains of the TF1-GFP-BCR-ABL cell shown in (a), color coded according to the value of $\mathcal{M}_\psi[\Phi]$; (e) plot of the argument $\mathcal{A}_\psi[\Phi]_{\text{WTMM}}$ of the WTMM chains versus θ [same color coding as in (d)]; and (f) plot of $\Delta\theta = \mathcal{A}_\psi[\Phi]_{\text{WTMM}} - \theta$ versus θ .

cell and 0.035 ± 0.02 for TF1-GFP-BCR-ABL cell) than along the outer contour ($\mathcal{M}_\psi[\Phi] = 0.061 \pm 0.047$ for TF1-GFP cell and 0.07 ± 0.0085 for TF1-GFP-BCR-ABL cell). This internal reorganization of the TF1-GFP-BCR-ABL is also visible on the higher dispersion of the WT arguments [Figs. 8(e) and 8(f) and 9(e) and 9(f)]. If this preliminary discussion on these two cells does not allow us to make general conclusions on the transformation of TF1 cells upon BCR-ABL oncogen transduction, it

simply illustrates the fact that the internal structure of these cells may appear very different through QPM analysis.

We repeated this analysis on two large sets of TF1-GFP (294) and TF1-GFP-BCR-ABL (216) cells, and we computed the statistical distributions of the mean radius of the outer chain, the OPV, the mean RI drop [computed from Eq. (20)], the angle difference $\Delta\theta$, the number of chains per cells, and the chain length (Fig. 10). The cell radius distribution is clearly shifted

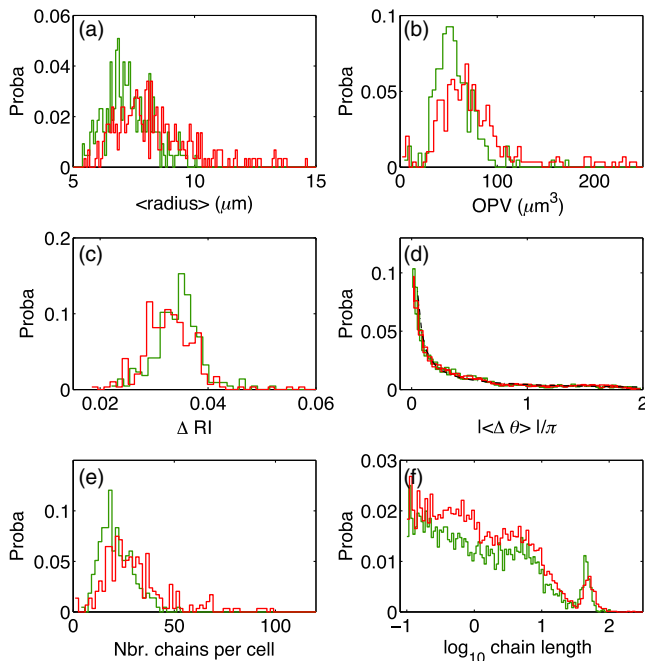


Fig. 10 Statistical analysis of cell structural parameters from the WTMM analysis of the OPD of control and cancer cell lines: (a) distribution of mean cell radius, estimated from the outermost contour WTMM chain; (b) distributions of OPVs computed from Eq. (19); (c) distributions of RI drops computed from Eq. (20); (d) distribution of $\Delta\theta$ values; (e) distribution of the numbers of chains per cell; $\overline{N_C} = 21 \pm 7$ for TF1-GFP cells and $\overline{N_C} = 30 \pm 9$ for TF1-GFP-BCR-ABL cells; and (f) distribution of chain lengths (\log_{10} of the length in μm). The green (respectively red) lines are obtained from a set of 294 (respectively 216) TF1-GFP (respectively TF1-GFP-BCR-ABL) cells.

and spread to larger values with $\overline{R_C} = 7.2 \pm 1.2 \mu\text{m}$ for the TF1-GFP cells and $\overline{R_C} = 8.2 \pm 2.1 \mu\text{m}$ for the TF1-GFP-BCR-ABL cells. The OPV follows the same trend with $\overline{\text{OPV}} = 56 \pm 3 \mu\text{m}^3$ for the TF1-GFP cells and $\overline{\text{OPV}} = 89 \pm 5 \mu\text{m}^3$ for the TF1-GFP-BCR-ABL cells (we use the error of the mean for these quantities). Again, we note that the OPV values are much more dispersed for the transformed cells. The oncogene transduction seems to increase the variability of the cell structural properties. One more surprising result is that the mean RI drop (inner to outer media) of these cells is slightly decreasing from 0.0351 ± 0.0075 to 0.0331 ± 0.019 , suggesting that the apparent swelling of the TF1-GFP-BCR-ABL cells is not followed by an adapted increase of the intracellular concentration of proteins to keep the mean RI invariant. The distribution of angle differences $\Delta\theta$ follows a power law distribution $P(\Delta\theta) \propto |\Delta\theta|^{-\alpha}$, with $\alpha = 1$. The fact that the shape of this distribution does not change when switching from control to oncogene-transduced TF1 cell means that the statistics of angular orientation of the maxima chains are not immediately impacted by the cell transformation. In contrast, the number of chains per cell is affected by oncogene transduction. The median value of the two distributions in Fig. 10(e) increases from 21 to 30 chains per cell (considering only the chains of length larger than 100 nm). Again, we observe that the distribution of these chain numbers for TF1-GFP-BCR-ABL cells is more spread out than for control TF1-GFP cells. The distribution of length of these chains (above 100 nm) follows a smoothly decreasing (logarithmic decrease) function for chains smaller than 5 μm , which drops rapidly to zero for larger chains. The peak popping up

around 45 μm corresponds to the outer chain length, and the slight flattening and shifting to higher values of this peak for transduced TF1-GFP-BCR-ABL cells mean that the circumference of these cells increases (as their radius) and is more variable than for nontransformed cells. This observation corroborates our previous remarks on the cell radius distribution.

5 Conclusions

The interpretation of quantitative phase images of living cells and their inversion for recovering index profiles is a very tough task, since a living cell is rarely a homogeneous media, and even worse its internal bodies (cytoskeletal networks of filaments, endoplasmic reticulum, golgi, mitochondrial network, and intranuclear structures) are not invariant during the cell cycle. It is, therefore, very difficult to predict a well-established distribution of the RIs of a living cell. For instance, the integrated RI values over the cell thickness extracted from the phase images are not systematically organized along closed domains, strongly challenging traditional interpretation of phase images by phase isocontours. When the phase profiles are not monotonous nor smooth functions, the derivatives of the phase may display local maxima that reflect a local change of RI or the topography of the cells. We show here that the detection of these local maxima may help us deciphering the internal complexity of living cells. The introduction of the WTMM method to detect the maxima of the derivative of the phase allows a robust and automatized reconstruction of their outer and inner boundary chains. From these chains, morphological and global RI characterizations of living blood cells can be performed. The reported comparison of the results obtained for erythrocytes, primary immature hematopoietic (CD34+), and model (TF1) cells provides a good survey of the efficiency of this method to distinguish healthy from cancer cells. In particular, this study suggests that the RI and its intracellular roughening may serve as a quantitative marker for cancer cell detection.

Acknowledgments

We are very thankful to Centre National de la Recherche Scientifique, Ecole Normale Supérieure de Lyon, Lyon Science Transfert (project L659), Région Rhône Alpes (CIBLÉ Program 2011), INSERM (AAP Physique Cancer 2012), and the French Agency for Research (ANR-AA-PPPP-005, EMMA 2011, ANR-11 IDEX-0007-02 with the PRES-University of Lyon) for their financial support. C.M.T. is very grateful to the National Council of Science and Technology (CONACyT, Mexico) for supporting her PhD scholarship.

References

1. N. Lue et al., "Live cell refractometry using microfluidic devices," *Opt. Lett.* **31**, 2759–2761 (2006).
2. C. Brunner, A. Niendorf, and J. A. Käs, "Passive and active single-cell biomechanics: a new perspective in cancer diagnosis," *Soft Matter* **5**, 2171–2178 (2009).
3. G. Popescu, "Random and deterministic transport in live cells quantified by SLIM," in *OSA: BODANTM/OMP/OTA*, p. 1 (2011).
4. D. K. Kang et al., "Droplet microfluidics for single-molecule and single-cell analysis in cancer research, diagnosis and therapy," *Trends Anal. Chem.* **58**, 145–153 (2014).
5. A. Grünberger, W. Wiechert, and D. Kohlheyer, "Single-cell microfluidics: opportunity for bioprocess development," *Curr. Opin. Biotechnol.* **29**, 15–23 (2014).
6. G. Popescu, *Quantitative Phase Imaging of Cells and Tissues*, McGraw Hill, New York (2011).

7. K. Lee et al., "Quantitative phase imaging techniques for the study of cell pathophysiology: from principles to applications," *Sensors* **13**(4), 4170–4191 (2013).
8. C. L. Curl et al., "Refractive index measurement in viable cells using quantitative phase-amplitude microscopy and confocal microscopy," *Cytometry, Part A* **65**, 88–92 (2005).
9. B. Rappaz et al., "Measurement of the integral refractive index and dynamic cell morphology of living cells with digital holographic microscopy," *Opt. Express* **13**, 9361–9373 (2005).
10. W. Choi et al., "Tomographic phase microscopy," *Nat. Methods* **4**(9), 717–719 (2007).
11. W. J. Choi et al., "Full-field optical coherence microscopy for identifying live cancer cells by quantitative measurement of refractive index distribution," *Opt. Express* **18**(22), 23285–23295 (2010).
12. T. Yamauchi et al., "Low-coherent quantitative phase microscope for nanometer-scale measurement of living cells morphology," *Opt. Express* **16**, 12227–12238 (2008).
13. V. Backman et al., "Detection of preinvasive cancer cells," *Nature* **406**, 35–36 (2000).
14. X. Liang et al., "Determining refractive index of single living cell using an integrated microchip," *Sens. Actuators, A* **133**, 349–354 (2007).
15. Y. Park et al., "Refractive index maps and membrane dynamics of human red blood cells parasitized by *Plasmodium falciparum*," *Proc. Natl. Acad. Sci. U. S. A.* **105**, 13730–13735 (2008).
16. Y. Yanase et al., "Detection of refractive index changes in individual living cells by means of surface plasmon resonance imaging," *Biosens. Bioelectron.* **26**(2), 674–681 (2010).
17. P. Bon, B. Wattellier, and S. Monneret, "Modeling quantitative phase image formation under tilted illuminations," *Opt. Lett.* **37**, 1718–1720 (2012).
18. Y. Yanase et al., "Evaluation of peripheral blood basophil activation by means of surface plasmon resonance imaging," *Biosens. Bioelectron.* **32**(1), 62–68 (2012).
19. D. Morikawa et al., "Detection of swelling of single isolated mitochondrion with optical microscopy," *Biomed. Opt. Express* **5**(3), 848–857 (2014).
20. H. V. Pham et al., "Real time blood testing using quantitative phase imaging," *PLoS One* **8**, e55676 (2013).
21. V. P. Tychinsky et al., "Dissecting eukaryotic cells by coherent phase microscopy: quantitative analysis of quiescent and activated T lymphocytes," *J. Biomed. Opt.* **17**, 076020 (2012).
22. P. Marquet et al., "Digital holographic microscopy: a noninvasive contrast imaging technique allowing quantitative visualization of living cells with subwavelength axial accuracy," *Opt. Lett.* **30**(5), 468–470 (2005).
23. G. Popescu et al., "Diffraction phase microscopy for quantifying cell structure and dynamics," *Opt. Lett.* **31**, 775–777 (2006).
24. Y. Park et al., "Diffraction phase and fluorescence microscopy," *Opt. Express* **14**, 8263–8268 (2006).
25. B. Bhaduri et al., "Diffraction phase microscopy with white light," *Opt. Lett.* **37**, 1094–1096 (2012).
26. Y. Park et al., "Measurement of red blood cell mechanics during morphological changes," *Proc. Natl. Acad. Sci. U. S. A.* **107**, 6731–6836 (2010).
27. B. Rappaz et al., "Simultaneous cell morphometry and refractive index measurement with dual-wavelength digital holographic microscopy and dye-enhanced dispersion of perfusion medium," *Opt. Lett.* **33**, 744–746 (2008).
28. V. Lauer, "New approach to optical diffraction tomography yielding a vector equation of diffraction tomography and a novel tomographic microscope," *J. Microsc.* **205**(2), 165–176 (2002).
29. Y. Sung et al., "Optical diffraction tomography for high resolution live cell imaging," *Opt. Express* **17**(1), 266–277 (2009).
30. R. Fiolka et al., "Simplified approach to diffraction tomography in optical microscopy," *Opt. Express* **17**(15), 12407–12417 (2009).
31. K. Kim et al., "Diffraction optical tomography using a quantitative phase imaging unit," *Opt. Lett.* **39**(24), 6935–6938 (2014).
32. S. Shin et al., "Active illumination using a digital micromirror device for quantitative phase imaging," arXiv:1506.06237 (2015).
33. C. Hammond, "A symmetrical representation of the geometrical optics of the light microscope," *J. Microsc.* **192**(1), 63–68 (1998).
34. B. Laperrousaz et al., "Primitive CML cell expansion relies on abnormal levels of BMPs provided by the niche and on BMPRIb overexpression," *Blood* **122**(23), 3767–3777 (2013).
35. J. P. Antoine et al., *Two-Dimensional Wavelets and their Relatives*, Cambridge University Press, Cambridge, UK (2004).
36. C. Martinez-Torres et al., "Diffraction phase microscopy: retrieving phase contours on living cells with a wavelet-based space-scale analysis," *J. Biomed. Opt.* **19**, 036007 (2014).
37. J. Zhong and J. Weng, "Phase retrieval of optical fringe pattern from the ridge of a wavelet transform," *Opt. Lett.* **30**(19), 2560–2562 (2005).
38. Z. Wang and H. Ma, "Advanced continuous wavelet transform algorithm for digital interferogram analysis and processing," *Opt. Eng.* **45**, 045601 (2006).
39. S. Li, X. Su, and W. Chen, "Wavelet ridge techniques in optical fringe pattern analysis," *J. Opt. Soc. Am. A* **27**(6), 1245–1254 (2010).
40. J. Ma et al., "Two-dimensional continuous wavelet transform for phase determination of complex interferograms," *Appl. Opt.* **50**(16), 2425–2430 (2011).
41. T. Ikeda et al., "Hilbert phase microscopy for investigating fast dynamics in transparent systems," *Opt. Lett.* **30**, 1165–1167 (2005).
42. Y. Sung et al., "Stain-free quantification of chromosomes in live cells using regularized tomographic phase microscopy," *PLoS One* **7**, e49502 (2012).
43. S. Mallat and W. L. Hwang, "Singularity detection and processing with wavelets," *IEEE Trans. Inf. Theory* **38**(2), 617–643 (1992).
44. S. Mallat and S. Zhong, "Characterization of signals from multiscale edges," *IEEE Trans. Pattern Anal. Mach. Intell.* **14**(7), 710–732 (1992).
45. A. Arneodo, N. Decoster, and S. Roux, "A wavelet-based method for multifractal image analysis. I. Methodology and test applications on isotropic and anisotropic random rough surfaces," *Eur. Phys. J. B* **15**(3), 567–600 (2000).
46. N. Decoster, S. G. Roux, and A. Arneodo, "A wavelet-based method for multifractal image analysis. II. Applications to synthetic multifractal rough surfaces," *Eur. Phys. J. B* **15**(4), 739–764 (2000).
47. A. Arneodo et al., "A wavelet-based method for multifractal image analysis: from theoretical concepts to experimental applications," *Adv. Imaging Electron Phys.* **126**, 1–92 (2003).
48. J. Canny, "A computational approach to edge detection," *IEEE Trans. Pattern Anal. Mach. Intell.* **PAMI-8**(6), 679–698 (1986).
49. A. Khalil et al., "Chromosome territories have a highly nonspherical morphology and nonrandom positioning," *Chromosome Res.* **15**(7), 899–916 (2007).
50. A. Thaer, "The refractive index and dry mass distribution of mammalian erythrocytes," *J. Microsc.* **89**(2), 237–250 (1969).
51. A. Roggan et al., "Optical properties of circulating human blood in the wavelength range 400–2500 nm," *J. Biomed. Opt.* **4**(1), 36–46 (1999).
52. S. V. Tsinopoulos and D. Polyzos, "Scattering of He-Ne laser light by an average-sized red blood cell," *Appl. Opt.* **38**(25), 5499–5510 (1999).
53. Y. C. Fung and P. Tong, "Theory of the sphering of red blood cells," *Biophys. J.* **8**, 175–198 (1968).
54. Y. C. Fung, *Biomechanics: Mechanical Properties of Living Tissues*, Springer Verlag, New York (1993).
55. S. Wang et al., "Three-dimensional refractive index reconstruction of red blood cells with one-dimensional moving based on local plane wave approximation," *J. Opt.* **14**, 065301 (2012).
56. P. H. Wiernik, *Adult Leukemia*, BC Decker Inc., Hamilton, London (2001).
57. M. D. Huber and L. Gerace, "The size-wise nucleus: nuclear volume control in eukaryotes," *J. Cell Biol.* **179**(4), 583–584 (2007).
58. D. Zink, A. H. Fischer, and J. A. Nickerson, "Nuclear structure in cancer cells," *Nat. Rev. Cancer* **4**(9), 677–687 (2004).
59. S. Nazlibilek et al., "Automatic segmentation, counting, size determination and classification of white blood cells," *Measurement* **55**, 58–65 (2014).
60. R. Barer, "Refractometry and interferometry of living cells," *J. Opt. Soc. Am.* **47**, 545–556 (1957).
61. H. E. Broxmeyer et al., "Hematopoietic colony formation from human growth factor-dependent TF1 cells and human cord blood myeloid progenitor cells depends on Shp2 phosphatase function," *Stem Cells Dev.* **22**(6), 998–1006 (2012).
62. J. R. McWhirter and J. Y. J. Wang, "Activation of tyrosine kinase and microfilament-binding functions of c-ABL by BCR sequences in BCR-ABL fusion proteins," *Mol. Cell. Biol.* **11**(3), 1553–1565 (1991).
63. R. Salgia et al., "BCR/ABL induces multiple abnormalities of cytoskeletal function," *J. Clin. Invest.* **100**(1), 46–57 (1997).
64. J. R. McWhirter and J. Y. J. Wang, "An actin-binding function contributes to transformation by the BCR-ABL oncoprotein of Philadelphia chromosome-positive human leukemias," *EMBO J.* **12**, 1533–1546 (1993).

Cristina Martinez-Torres obtained her BSc in biophysics from the Autonomous University of San Luis Potosi, Mexico, in 2011. During her undergraduate studies, she was involved in several research groups, working in topics such as bioinformatics, cellular biology, biophysics, optical engineering, and atomic physics. Currently, she is a PhD student at the ENS Lyon, where she studies the structure and dynamics of single living cells.

Bastien Laperrousaz received his PhD in biology from the Ecole Normale Supérieure of Lyon, France, in 2015, at the interface with the Cancer Research Center of Lyon. He is currently developing microfluidic devices for high-throughput and high-content RNAi screens of 3D tumor structures for biomedical applications at the Institute of Life Sciences Research and Technologies of the Atomic Energy Commission, Grenoble, France. His research interests include cancer stem cell biology, biotechnologies, and biomedical applications.

Lotfi Berguiga received his PhD in physics from the University of Burgundy, Dijon, France, in 2001, where he worked in near field optics. Since 2004, he has worked at the Ecole Normale Supérieure de Lyon, where he has investigated surface plasmon microscopy. Since 2007, he has worked as research engineer at the French National Centre for Scientific Research, and his research interests include development of new techniques of microscopy applied to cell biology.

Elise Boyer-Provera graduated in optics and industrial visual systems from the Engineering School of Telecom in Saint Etienne, France, in 2010. After a three-year training in the private company Thales Angenieux, she was hired as an engineer at Ecole Normale Supérieure de Lyon to develop original microscopy devices based on surface plasmon microscopy and quantitative phase microscopy.

Juan Elezgaray received his PhD in theoretical physics from University of Paris 6, France, in 1989. Since 1989, he has been a researcher at CNRS. Currently, he works in the UMR 5248 (CBMN) unit in Pessac (France). He has collaborated with Françoise Argoul's team in the development of a surface plasmon microscope. His interests include the modelling of nano-optical systems and DNA nanotechnology.

Franck E. Nicolini got his PhD from University Claude Bernard, Lyon, France in 2001 and his "habilitation for directing research" in human biology in 2004, in the same university. He worked as a hospital

practitioner in the hematology department of Pr. J. Reiffers between 1999–2001, mostly focused on CML and autologous and allogeneic stem cell transplant. He is a senior scientist in the Inserm research unit 1042 in Lyon, where he leads with Dr. Maguer-Satta a scientific program of basic scientific research on CML and normal hematopoiesis, mostly focus on the role of the hematopoietic niche in the resistance of CML to TKIs and maintenance of Ph+ stem cells. He has more than 100 original publications and book chapters in the field of hematology, stem cell transplantation and CML, and is or has been a reviewer several times for more than 20 peer-reviewed journals in the field of hematology, and for EHA, EBMT, and ASH meetings.

Véronique Maguer Satta received her PhD in immune-virology at University Claude Bernard of Lyon 1, France (1994). She spent several years in Dr. C. Eaves' laboratory in Vancouver, Canada (1994–1997) to learn normal and leukemic hematopoiesis. Then she joined for one year Pr. Reiffers lab in Bordeaux, France, to explore a clinical approach of research in hematopoiesis. In 1998, she developed her own research group on human hematopoiesis at Inserm U453, Lyon, France. She was recruited by CNRS as a permanent researcher (2002) and promoted research director (2012). She is now directing her research team on "BMPs, tumor niche and cancer stem cells" at the Cancer Research Center of Lyon-CRCL, France.

Alain Arneodo received his thesis in elementary particle physics from the University of Nice, France, in 1978. Then he switched his scientific interests to complex systems. After 20 years in a Bordeaux (France) CNRS laboratory, he moved to ENS Lyon (France) to work at the physics-biology interface. His scientific contribution encompasses many fields of modern physics including statistical mechanics, dynamical systems theory, chaos, fully-developed turbulence, economics, geophysics, the mathematics of fractals and multifractals, fractal growth phenomena, signal and image processing, multi-scale analysis based on wavelets.

Françoise Argoul received her PhD from the University of Bordeaux, France, in 1986. She was promoted director of research (CNRS) in 1997 and has coauthored over 130 peer-reviewed papers. She manages a research program in Physics Department of ENS Lyon (France), devoted to the experimental characterization of the mechanical and genomic response of cellular systems under external stress. Her expertise ranges from nonlinear and complex dynamical systems to nanomechanical and optomechanical methods for capturing the dynamics of living systems.